

Understanding the quantum Rabi ring using analogies to quantum magnetism

Diego Fallas Padilla* and Han Pu†

*Department of Physics and Astronomy, and Rice Center for Quantum Materials,
Rice University, Houston, Texas 77251-1892, USA*

Guo-Jing Cheng and Yu-Yu Zhang‡

*Department of Physics, and Chongqing Key Laboratory for strongly coupled Physics,
Chongqing University, Chongqing 401330, China*

(Dated: July 19, 2022)

We map a quantum Rabi ring, consisting of N cavities arranged in a ring geometry, into an effective magnetic model containing the XY exchange and the Dzyaloshinskii-Moriya (DM) interactions. The analogue of the latter is induced by an artificial magnetic field, which modulates photon hopping between nearest-neighbor cavities with a phase. The mean-field behavior of both systems is almost identical, facilitating the description of the different phases in the quantum optical model through simple arguments of competing magnetic interactions. For the square geometry ($N = 4$) the rich phase diagram exhibits three superradiant phases denoted as ferro-superradiant, antiferro-superradiant and chiral superradiant. In particular, the DM interaction is responsible for the chiral phase in which the energetically degenerate configurations of the order parameters are similar to the in-plane magnetizations of skyrmions with different helicities. The antiferro-superradiant phase is suppressed in the triangle geometry ($N = 3$) as geometric frustration contributes to stabilize the chiral phase even for small values of the DM interaction. The chiral phases for odd and even N show a different scaling behavior close to the phase transition. The equivalent behavior on both systems opens the possibility of simulating chiral magnetism in a few-body quantum optical platform, as well as understanding one system using the insights gained from the other.

Introduction – It is not unusual that two seemingly very different systems are connected by the same underlying physics. Finding such connections can often help us to gain new insights into one system by importing knowledge obtained from the study of the other. Here we show how a light-matter interaction system — the quantum Rabi ring — can be mapped to a chiral magnetic system consisting of various kinds of magnetic couplings including, for example, the Dzyaloshinskii-Moriya (DM) interaction [1, 2] which plays a fundamental role in the study of topological states in magnetic systems, see for example [3]. The DM interaction favors non-collinear spin structures, stabilizing interesting spin textures such as magnetic skyrmions in chiral magnets [4–6] which have been observed experimentally, for example, in helimagnets under the presence of an external magnetic field [7, 8]. Alongside with the DM interaction, other mechanisms that can stabilize chiral spin textures are perpendicular easy-axis anisotropy, geometric frustration, or a combination of all the aforementioned [9, 10]. Although such interesting behaviors have been observed in magnetic solid state materials, exploring a wide range of exchange interaction strengths in a single experiment might not be an easy task, indicating the relevance of finding other highly controllable experimental platforms where magnetic systems could be simulated.

Light-matter interaction systems have been used extensively to explore many-body quantum phases in dif-

ferent platforms such as cavity and circuit QED [11–14], and cold atoms in optical lattices [15–17]. High tunability and control in these experimental environments makes them attractive candidates to simulate condensed matter magnetic systems. For example, cold atoms in optical lattices have been used to simulate antiferromagnetic spin chains [18] and frustrated classical magnetism [19], while an optical cavity has been used to engineer collective spin exchange interactions [20].

On top of the already interesting interactions between cavity modes and atoms, other intriguing many-body phases of quantum systems can be achieved when the presence of external fields is added to the mix. Recent experimental advances and theoretical findings have addressed synthesizing magnetic fields for neutral ultracold atoms [21–23] and photonic systems [16, 24–27]. In particular, addition of artificial magnetic fields have been proven to unlock the emergence of exotic phases of matter, such as chiral ground-state currents of interacting photons in a three-qubit loop [26], chiral phases in a quantum Rabi triangle [28], and fractional quantum Hall physics in the Jaynes-Cummings Hubbard lattice [29–31]. Observation of these stable chiral phases in optical setups serves as a further motivation to draw connections between these phenomena and chiral magnetism.

Here we study a quantum Rabi ring and show that it can be mapped into a large-spin magnetic Hamiltonian of Lipkin-Meshkov-Glick (LMG) systems with nearest-neighbor interactions. Through this mapping, the different phases in the quantum Rabi ring can be intuitively understood by studying the competition of the DM interaction and the XY Heisenberg exchange interaction

* daf5@rice.edu

† hpu@rice.edu

‡ yuyuzh@cqu.edu.cn

in the equivalent LMG ring. Furthermore, we also show that the behavior of the chiral phases is highly influenced by geometric frustration.

Quantum Rabi ring – We consider a system with N cavities placed in a ring. Each cavity contains a two-level atom and is described by the quantum Rabi Hamiltonian

$$H_{R,n} = \omega a_n^\dagger a_n + g(a_n^\dagger + a_n)\sigma_n^x + \frac{\Delta}{2}\sigma_n^z, \quad (1)$$

where a_n (a_n^\dagger) is the photon annihilation (creation) operator of the single-mode cavity with frequency ω at cavity n , g is the atom-cavity coupling strength, and σ_n^i are the Pauli matrices representing the two-level atom at site n with energy splitting Δ between levels. The dimensionless coupling strength is defined as $g_1 \equiv g/\sqrt{\Delta\omega}$.

Although quantum phase transitions (QPTs) are often studied in the thermodynamic limit of infinite lattice sites (or infinite number of atoms) [32], some few-body systems such as the quantum Rabi model [33–37] or the Jaynes-Cummings finite lattice systems [38] have been proven to undergo photon QPTs in alternative limits such as the classical oscillator (CO) limit with $\Delta/\omega \rightarrow \infty$ [39]. This is the regime we will focus on in this work.

The quantum Rabi ring Hamiltonian contains photon hopping between the neighboring cavities

$$H_{RR} = \sum_{n=1}^N H_{R,n} + \sum_{n=1}^N J(e^{i\theta} a_n^\dagger a_{n+1} + e^{-i\theta} a_{n+1}^\dagger a_n), \quad (2)$$

where J is the hopping amplitude between nearest-neighbor cavities with a phase θ , and periodic boundary condition implies $a_{N+1} = a_1$. A thorough description of this system in a triangle ($N = 3$) can be found in [28]. An artificial vector potential $A(r)$ leads the photon hopping terms between nearby cavities n and m to become complex with the phase given by $\theta = \int_{r_n}^{r_m} A(r)dr$. The sum of the phases along the closed loop of the N cavities $N\theta$ is equivalent to the effective magnetic flux. The artificial magnetic field can be realized by a periodic modulation of the photon hopping strength dependent on cavities with tunable resonances [26, 28]. The complex phase breaks time-reversal symmetry (TRS) and, as will be shown, is crucial in leading to the DM interaction in the mapped magnetic model.

In the classical oscillator limit $\Delta/\omega \rightarrow \infty$, the quantum Rabi model in each cavity undergoes a quantum phase transition from a normal phase to a superradiant phase [34, 38, 40]. For small values of g_1 , the average number of photons in the cavity tends to zero, which is the so-called normal phase. As g_1 increases to the critical point g_{1c} , the photon population on each cavity becomes macroscopic (proportional to $\frac{\Delta}{\omega}$), signaling the superradiant phase. Moreover, the hopping of photons between neighboring cavities unlocks more exotic superradiant phases with the order parameter $\langle a_n \rangle$ being site-dependent.

A general description of the mean-field features and excitation spectrum of this model can be done by constructing low-energy effective Hamiltonians for each phase (see Supplemental Material [41]). After shifting the bosonic operator $a_n \rightarrow \tilde{a}_n + \alpha_n$ with the complex mean-field value $\alpha_n = A_n + iB_n$, the effective low-energy Hamiltonian under the condition $J/\omega \ll 1$ is obtained by projecting to the spin subspace $|\downarrow\rangle$, giving

$$H_{\text{eff}}^\downarrow = \sum_{n=1}^N \left[\omega \tilde{a}_n^\dagger \tilde{a}_n - \frac{\lambda_n^2}{\Delta_n} (\tilde{a}_n^\dagger + \tilde{a}_n)^2 + J \tilde{a}_n^\dagger (e^{i\theta} \tilde{a}_{n+1} + e^{-i\theta} \tilde{a}_{n-1}) \right] + E_g, \quad (3)$$

where $\Delta_n \equiv \sqrt{\Delta^2 + 16g^2A_n^2}$, $\lambda_n \equiv g\Delta/\Delta_n$, and the mean-field ground-state energy E_g is given by

$$E_g = \sum_{n=1}^N \left[\omega(A_n^2 + B_n^2) - \frac{1}{2} \sqrt{\Delta^2 + 16g^2A_n^2} + 2J \cos \theta (A_n A_{n+1} + B_n B_{n+1}) + 2J \sin \theta (B_n A_{n+1} - B_{n+1} A_n) \right]. \quad (4)$$

Minimization of E_g with respect to A_n and B_n (see Supplemental Material) yields the condition $\omega B_n + J \sin \theta (A_{n+1} - A_{n-1}) + J \cos \theta (B_{n+1} + B_{n-1}) = 0$. Furthermore, when N is odd, there are additional conditions $B_N = -B_1$ and $A_N = A_1$ that need to be satisfied. This indicates the qualitative difference between even and odd N . As we will show later, odd N gives rise to geometric frustration. Finally, we want to stress that, in the absence of the artificial magnetic field (i.e., $\theta = 0$ or $\pm\pi$), $B_n = 0$ for all n .

Effective magnetic model: LMG ring – We now map the effective Hamiltonian (3) using the Holstein-Primakoff transformation [42] given by $S^z = a^\dagger a - S$ and $S_n^+ = a_n^\dagger \sqrt{2S - a_n^\dagger a_n}$. In the normal phase $\langle a_n \rangle = A_n + iB_n = 0$ and in the classical spin limit $S \rightarrow \infty$, the Holstein-Primakoff transformation can be approximated by $S_n^+ \approx \sqrt{2S} a_n^\dagger$, leading to the magnetic Hamiltonian

$$H_{\text{LMGR}} = \sum_{n=1}^N \left[\omega S_n^z - \frac{2g_1^2\omega}{S} (S_n^x)^2 \right] + \frac{J}{S} \cos \theta \sum_{n=1}^N (S_n^x S_{n+1}^x + S_n^y S_{n+1}^y) + \frac{J}{S} \sin \theta \sum_{n=1}^N \hat{z} \cdot (\vec{S}_n \times \vec{S}_{n+1}), \quad (5)$$

which is also valid for the region in the superradiance phase not too far away from the normal-superradiance phase boundary. We denote H_{LMGR} as the LMG ring model as it is a generalization of the LMG Hamiltonian [43] with additional nearest-neighbor interactions included. The physical meaning of each term in H_{LMGR} is quite clear: The two terms in the first line represent an external magnetic along the z -axis and the easy-axis anisotropy along the x -axis, respectively; the second line

is a typical XY spin exchange interaction which is either ferromagnetic or antiferromagnetic depending on the sign of $J \cos \theta$; finally, the last line corresponds to the DM interaction with the strength $J \sin \theta$. The relative strength between the XY and the DM terms is thus controlled by θ .

Treating \vec{S} as a classical vector, the mean-field energy according to H_{LMGR} can be readily derived as

$$\begin{aligned} \frac{E_{MF}}{\omega S} = & \sum_{n=1}^N -\sqrt{(1 - X_n^2 - Y_n^2)} - 2g_1^2 X_n^2 \\ & + \frac{J}{\omega} \cos \theta (X_n X_{n+1} + Y_n Y_{n+1}) \\ & + \frac{J}{\omega} \sin \theta (X_n Y_{n+1} - X_{n+1} Y_n), \end{aligned} \quad (6)$$

where we have defined $X_n = \frac{\langle S_n^x \rangle}{S}$ and $Y_n = \frac{\langle S_n^y \rangle}{S}$. Minimization E_{MF} with respect to X_n and Y_n yields the ground-state phase diagram. One example with $N = 4$ is shown in Fig. 1(a). The phase diagram is presented in the θ - g_1 parameter space for fixed $J = 0.05\omega$. We only consider $\theta \in [0, \pi]$. The phase diagram in the range $\theta \in [-\pi, 0]$ is a mirror image of the one presented here.

For small g_1 , the system is in the paramagnetic phase (PP) where the spin is polarized by external field term along the z -axis. The PP is the analog of the normal phase in the original Rabi ring model. When g_1 exceeds a critical value, the system enters various non-paramagnetic phases according to the value of θ through a second-order phase transition. Defining two critical values of θ as

$$\cos \theta_c^\pm = \pm \frac{1 - \sqrt{1 + 16J^2/\omega^2}}{4J/\omega} \approx \mp 2J/\omega, \quad (7)$$

the non-paramagnetic phases can be characterized as:

1. Ferromagnetic Phase (FP) — For $\theta \in (\theta_c^+, \pi]$, and $g_1 > g_{1c}^+ = \frac{1}{2}\sqrt{1 + \frac{2J}{\omega} \cos \theta}$, the system enters the FP. Here the XY coupling is ferromagnetic. Together with the easy-axis anisotropy term, it polarizes the spin along either the x - or the $(-x)$ -axis. The ground state in FP is doubly degenerate as a result of the break of the Z_2 symmetry.
2. Antiferromagnetic Phase (AFP) — For $\theta \in [0, \theta_c^-)$, and $g_1 > g_{1c}^{\text{AF}} = \frac{1}{2}\sqrt{1 - \frac{2J}{\omega} \cos \theta}$, the system enters the AFP. Here the XY coupling is antiferromagnetic. The spins are polarized along the $(\pm x)$ -axis and neighboring spins are anti-aligned. The ground state in AFP is also doubly degenerate.
3. Chiral Magnetic Phase (CP) — In between FP and AFP, for $\theta \in (\theta_c^-, \theta_c^+)$ and $g_1 > g_{1c}^{\text{C}} = \frac{1}{2}\sqrt{1 + \frac{4J^2}{\omega^2} \sin^2 \theta}$, the DM term dominates over the XY coupling and renders spins at different sites no

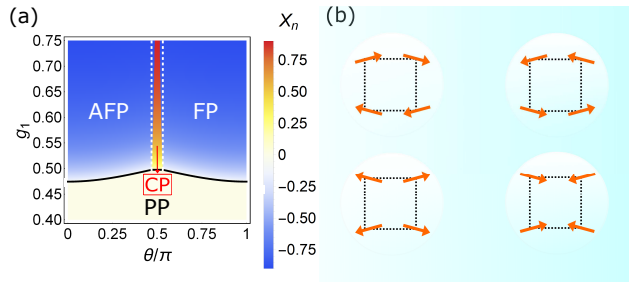


Figure 1. (a) Phase diagram in the θ - g_1 plane for the LMG ring with $N = 4$ using X_n for a given site n as order parameter. To facilitate visualization of the different phases we have chosen one of the degenerate configurations of the ground state for each phase, such that X_n in the chiral phase has opposite sign. The solid black line represents the second-order phase boundary, while vertical dashed lines represent the predicted first-order lines obtained from the equivalent quantum Rabi ring. The hopping strength is set to $J/\omega = 0.05$. (b) Allowed magnetization configurations in the CP for $N = 4$ represented in the xy -plane.

Table I. Correspondence between phases in the quantum Rabi ring (QRR) and those in the LMG ring (LMGR).

QRR phase	LMGR phase
Normal (NP): $A_n = B_n = 0$	Paramagnetic (PP): $X_n = Y_n = 0$
Ferro-superradiant (FSP): $B_n = 0$ and $A_n = A_{n+1}$	Ferromagnetic (FP): $Y_n = 0$ and $X_n = X_{n+1}$
Antiferro-superradiant (AFSP): $B_n = 0$ and $A_n = -A_{n+1}$	Antiferromagnetic (AFP): $Y_n = 0$ and $X_n = -X_{n+1}$
Chiral superradiant (CSP): $B_n \neq 0$ and $A_n \neq 0$	Chiral magnetic (CP): $Y_n \neq 0$ and $X_n \neq 0$

longer collinear. Here the ground state is 4-fold degenerate, breaking both the Z_2 and the C_4 symmetries, and the corresponding in-plane magnetization orientation in the xy -plane is shown in Fig. 1(b).

Note that the transitions between various non-paramagnetic phases are all of first order, and the critical points at θ_c^\pm are triple points where three phases (PP, FP/AFP, and CP) coexist.

Each magnetic phase described in terms of the values of X_n and Y_n , has an equivalent phase in the quantum Rabi ring in terms of A_n and B_n , as shown in Table I. A similar phase diagram as in Fig. 1(a) would be obtained if we solve the quantum Rabi ring Hamiltonian (3) directly. In particular, the second-order phase boundary between the normal and the superradiant phases is exactly the same as the boundary between the paramagnetic and non-paramagnetic phases. The first-order phase boundaries between different superradiant phases slightly deviates from those between different non-paramagnetic phases for large g_1 far away from the second-order boundary.

The similarity in the mean-field behavior of both systems indicates the possibility of simulating magnetic behavior using the quantum Rabi ring. In addition to re-

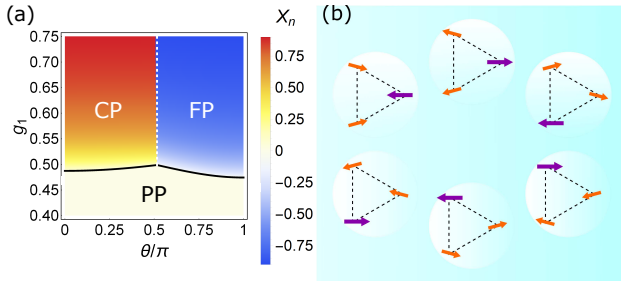


Figure 2. (a) Phase diagram in the θ - g_1 plane for the LMG ring with $N = 3$ using X_n for a given site n as order parameter. To facilitate visualization of the different phases we have chosen one of the degenerate configurations of the ground state for each phase, such that X_n in the chiral phase has opposite sign. The solid black line represents the second-order phase boundary, while vertical dashed lines represent the predicted first-order lines obtained from the equivalent quantum Rabi ring. The hopping strength is set to $J/\omega = 0.05$. (b) Allowed magnetization configurations in the CP for $N = 3$ represented in the xy -plane. A similar schematic representation can be done for α_n in the complex plane. Arrows with different color and length represent sites with different in-plane magnetization length $l_n = \sqrt{X_n^2 + Y_n^2}$.

alizing various types of magnetic coupling terms, we can also simulate geometric frustration by changing N from even to odd. To this end, let us consider a triangular system with $N = 3$. Such an arrangement with antiferromagnetic coupling is a prototypical system that exhibits magnetic frustration.

Following the same procedure, we can obtain the phase diagram for $N = 3$ as shown in Fig. 2(a). We can use the same conceptual reasoning of competing magnetic interactions to understand the phase diagram of this particular geometry. The FP has identical expressions for the second-order phase boundary and order parameter values as the ones found for $N = 4$. The region of AFP phase is significantly reduced. In fact, AFP only occurs along the line $\theta = 0$. Along this line, the DM interaction vanishes exactly and the spins are aligned in the x -direction with the behavior being exactly the one of a classical frustrated anti-ferromagnet described by a Heisenberg model, as pointed out recently [44].

The CP is much broader in the triangular case as it is defined in the region where $0 < \theta \leq \theta_c = \cos^{-1}\left(-\frac{2J}{\sqrt{8J^2 + \omega^2} + \omega}\right)$ [28]. The ground state in the CP is 6-fold degenerate due to the break of both the Z_2 and the C_3 symmetries. The in-plane magnetization orientation of the degenerate CP states are shown in Fig. 2(b). In the previous square case, the spins at different sites point along different directions, but all have the same length. This is not the case in the triangular case. As one can see from Fig. 2(b), there is always a site where the transverse spin is along the x - or $(-x)$ -axis and this spin has larger magnitude than the other two. In the triangular quantum Rabi ring model, this means that the photon numbers at different sites are not the same. This

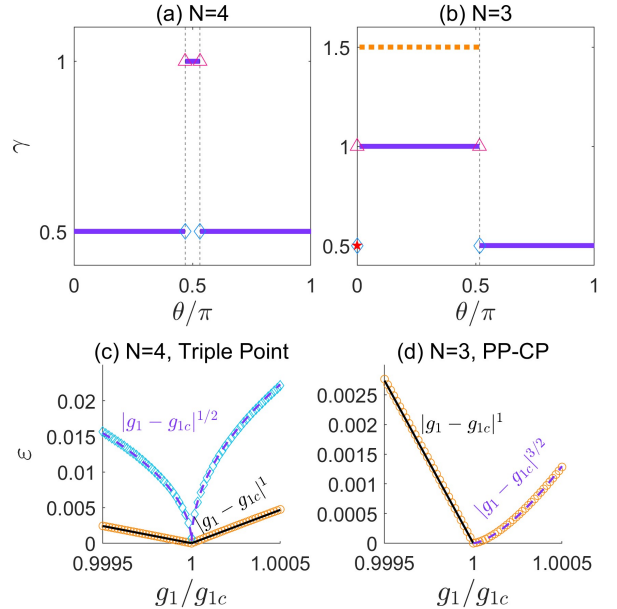


Figure 3. Scaling exponents γ as a function of θ for (a) $N = 4$ and (b) $N = 3$, vertical dashed lines indicate the boundary between non-paramagnetic phases. At the triple points, two modes vanish at the critical point with distinct exponents indicated as open markers. The PP-CP transition for $N = 3$ has non-symmetric exponents, the blue solid and the orange dashed line indicate the exponent when g_1 approaches the critical value from below and above, respectively. (c) Lowest and second-lowest excitation energies as a function of g_1/g_{1c} across the triple point at $\theta = \theta_c^+$. (d) Lowest excitation energy as a function of g_1/g_{1c} across the PP and the CP boundary for $N = 3$. The hopping strength is set to $J/\omega = 0.05$, and $\omega = 1$.

has important consequences in the excitation spectrum as we will show later. Also note that, for small values of θ , the XY exchange interaction $J \cos \theta > 0$ is stronger than the DM interaction, however, the system still favors a chiral phase with non-collinear alignment. This is very much in line with observations in antiferromagnetic systems [9, 45, 46] where geometric frustration has been proven to stabilize chiral spin textures favored by the DM interaction, even for very small values of the DM interaction coupling strength.

Excitation energy scaling – To characterize the differences between chiral phase transitions with and without frustration, in particular the consequences of the site-dependent magnetization length $l_n = \sqrt{X_n^2 + Y_n^2}$ for $N = 3$ shown in Fig.2(b), we analyze the excitation energy behavior near the transition for $N = 3$ and $N = 4$. The effective Hamiltonian in Eq. (3) can be diagonalized as $H_{RSL} = \sum_{n=1}^N \varepsilon_n b_n^\dagger b_n$ [41], where ε_n is the excitation energy of the n -th mode and b_n (b_n^\dagger) are bosonic annihilation (creation) operators of such mode obtained through a Bogoliubov transformation. Across a second-order phase boundary we expect the lowest excitation energy ε_1 to vanish exactly at the critical point, with a

power-law behavior of the form $\varepsilon_1 \propto |g_1 - g_{1c}|^\gamma$ around the critical point g_{1c} . Usually, it is expected that the value of γ is independent of whether the critical point is approached from above or below. However, as discussed below, this is not the case for the frustrated phases.

The scaling exponents γ as a function of θ are shown in panels (a) and (b) of Fig. 3 for $N = 4$ and $N = 3$, respectively. For $N = 4$ the scaling exponents before and after the transition are always equal to each other. The PP-FP and PP-AFP transitions have the same scaling exponent $\gamma = 1/2$, which is the same as the conventional single-cavity Dicke transition [47]. By contrast, $\gamma = 1$ for the PP-CP transition. At the triple point, two modes should vanish at the critical point as a signature of the co-existence of both non-paramagnetic phases, see Fig. 3(c). These modes possess exponents 1 and $1/2$, respectively, as indicated by the open markers in panel (a).

For $N = 3$ in the PP-FP transition $\gamma = 1/2$ just as in the $N = 4$ case. However, the PP-CP has an unusual scaling behavior as a consequence of the frustrated ground state configurations. As shown in panel (b) and in more detail in panel (d), the exponents at the two sides of the phase transition are different: $\gamma = 1$ ($= 1.5$) for g_1 approaching g_{1c} from below (above). At the triple point, we again have two modes vanishing at the critical point, each of which has a well defined scaling exponent, given by $\gamma = 1$ and $\gamma = 1/2$, just as for $N = 4$.

The difference in the scaling behavior of the CSP for $N = 3$ and $N = 4$ can be understood by exploring Eq.3, used to obtain the diagonalized Hamiltonian. For $N = 3$ the Hamiltonian in Eq.3, is C_3 symmetric for $g_1 < g_{1c}$ as λ_n/Δ_n is independent of n , however, for $g_1 > g_{1c}$ one of the sites has a different value of λ_n/Δ_n , breaking the symmetry. For $N = 4$, on the other hand, A_n^2 is independent of n in all phases, and consequently, Eq. (3) is always C_4 symmetric for both normal/paramagnetic and superradiant/non-paramagnetic phases.

This non-symmetric scaling behavior as a consequence of frustration has been reported for the special point $\theta = 0$ [44] where two modes vanish at the critical point, one with a single exponent $1/2$ and the other with non-symmetric exponents $\gamma = 1/2$ and $\gamma = 1$ below and above the transition, these three exponents are signaled with open markers in panel (b). This is consistent with our

results as the point $\theta = 0$ in our model where θ is a variable represents a triple point between the frustrated AFP and the frustrated CP, then, the vanishing of two modes is expected. Moreover, the non-symmetric γ values ($1/2$ and 1) at this point are different from the ones inside the CP region (1 and 1.5) as the ground-state configurations at $\theta = 0$ are not chiral, even though they are still frustrated.

Conclusions – We have explored the connection between the quantum Rabi ring model and a large-spin magnetic model (LMG ring) containing the XY Heisenberg exchange interactions and the DM interactions. The mapping between the two systems facilitates a deeper understanding of the phases in the light-atom coupling system through simple arguments of competing magnetic interactions, allowing us to connect each phase in the quantum Rabi ring to an equivalent magnetic phase in the LMG ring (Table I). For a square lattice ($N = 4$), in the region where the DM interaction dominates, a chiral superradiant phase (CSP) is observed. In this phase $\alpha_n = A_n + iB_n$ has an orientation that follows typical in-plane magnetization patterns observed in skyrmions with different helicities, when represented in the complex plane. Although both $N = 4$ and $N = 3$ possess a CSP, we find that the phase transitions leading to them are different from each other as indicated by the associated scaling exponents before and after the transition. The presence of geometric frustration for $N = 3$ is the key in this distinctive behavior as it stabilizes the chiral phase for a broader region and causes a site-dependent mean-field photon population $|\alpha_n|^2$. This work opens new possibilities on simulation of magnetic systems using quantum optical platforms. In particular, the classical oscillator limit considered here, facilitates the study of systems consisting of only a few (small N) spins, which can be a powerful tool for identifying the building blocks of more complex behaviors in real materials.

H.P. acknowledges support from the US NSF and the Welch Foundation (Grant No. C-1669). Y.Y.Z. acknowledges support from NSFC under Grant No.12075040 and No. 12147102, Chongqing NSF under Grants No. cstc2020jcyj-msxmX0890, and Fundamental Research Funds for the Central Universities Grant No. 2021CDJQY-007.

-
- [1] I. Dzyaloshinsky, Journal of physics and chemistry of solids **4**, 241 (1958).
 - [2] T. Moriya, Physical review **120**, 91 (1960).
 - [3] N. Nagaosa and Y. Tokura, Nature nanotechnology **8**, 899 (2013).
 - [4] A. Bogdanov and D. Yablonskii, Zh. Eksp. Teor. Fiz **95**, 182 (1989).
 - [5] A. Bogdanov and A. Hubert, Journal of magnetism and magnetic materials **138**, 255 (1994).
 - [6] U. K. Roessler, A. Bogdanov, and C. Pfleiderer, Nature **442**, 797 (2006).
 - [7] S. Mühlbauer, B. Binz, F. Jonietz, C. Pfleiderer, A. Rosch, A. Neubauer, R. Georgii, and P. Böni, Science **323**, 915 (2009).
 - [8] X. Yu, Y. Onose, N. Kanazawa, J. H. Park, J. Han, Y. Matsui, N. Nagaosa, and Y. Tokura, Nature **465**, 901 (2010).
 - [9] S. Hayami, S.-Z. Lin, and C. D. Batista, Physical Review B **93**, 184413 (2016).
 - [10] A. Leonov and M. Mostovoy, Nature communications **6**, 1 (2015).
 - [11] A. D. Greentree, C. Tahan, J. H. Cole, and L. C. Hollen-

- berg, *Nature Physics* **2**, 856 (2006).
- [12] M. J. Hartmann, F. G. Brandao, and M. B. Plenio, *Nature Physics* **2**, 849 (2006).
- [13] C. Zhu, L. Ping, Y. Yang, and G. S. Agarwal, *Physical Review Letters* **124**, 073602 (2020).
- [14] S. Felicetti and A. Le Boité, *Physical Review Letters* **124**, 040404 (2020).
- [15] I. Bloch, J. Dalibard, and W. Zwerger, *Reviews of modern physics* **80**, 885 (2008).
- [16] H. Cai and D.-W. Wang, *National science review* **8**, nwaa196 (2021).
- [17] X. Chen, Z. Wu, M. Jiang, X.-Y. Lü, X. Peng, and J. Du, *Nature communications* **12**, 1 (2021).
- [18] J. Simon, W. S. Bakr, R. Ma, M. E. Tai, P. M. Preiss, and M. Greiner, *Nature* **472**, 307 (2011).
- [19] J. Struck, C. Ölschläger, R. Le Targat, P. Soltan-Panahi, A. Eckardt, M. Lewenstein, P. Windpassinger, and K. Sengstock, *Science* **333**, 996 (2011).
- [20] M. A. Norcia, R. J. Lewis-Swan, J. R. Cline, B. Zhu, A. M. Rey, and J. K. Thompson, *Science* **361**, 259 (2018).
- [21] Y.-J. Lin, R. L. Compton, K. Jiménez-García, J. V. Porto, and I. B. Spielman, *Nature* **462**, 628 (2009).
- [22] J. Dalibard, F. Gerbier, G. Juzeliūnas, and P. Öhberg, *Reviews of Modern Physics* **83**, 1523 (2011).
- [23] H. Cao, Q. Wang, and L.-B. Fu, *Physical Review A* **89**, 013610 (2014).
- [24] R. Umucalılar and I. Carusotto, *Physical Review Letters* **108**, 206809 (2012).
- [25] D.-W. Wang, H. Cai, R.-B. Liu, and M. O. Scully, *Physical Review Letters* **116**, 220502 (2016).
- [26] P. Roushan, C. Neill, A. Megrant, Y. Chen, R. Babush, R. Barends, B. Campbell, Z. Chen, B. Chiaro, A. Dunsworth, *et al.*, *Nature Physics* **13**, 146 (2017).
- [27] I. Bloch, J. Dalibard, and S. Nascimbene, *Nature Physics* **8**, 267 (2012).
- [28] Y.-Y. Zhang, Z.-X. Hu, L. Fu, H.-G. Luo, H. Pu, X.-F. Zhang, *et al.*, *Physical Review Letters* **127**, 063602 (2021).
- [29] A. L. Hayward, A. M. Martin, and A. D. Greentree, *Physical Review Letters* **108**, 223602 (2012).
- [30] A. L. Hayward and A. M. Martin, *Physical Review A* **93**, 023828 (2016).
- [31] C. Noh and D. G. Angelakis, *Reports on Progress in Physics* **80**, 016401 (2016).
- [32] S. Sachdev, *Quantum Phase Transitions*, 2nd ed. (Cambridge University Press, 2011).
- [33] M.-J. Hwang, R. Puebla, and M. B. Plenio, *Physical review letters* **115**, 180404 (2015).
- [34] M. Liu, S. Chesi, Z.-J. Ying, X. Chen, H.-G. Luo, and H.-Q. Lin, *Physical Review Letters* **119**, 220601 (2017).
- [35] X.-Y. Chen, Y.-Y. Zhang, L. Fu, and H. Zheng, *Physical Review A* **101**, 033827 (2020).
- [36] D. Braak, *Physical Review Letters* **107**, 100401 (2011).
- [37] Q.-H. Chen, C. Wang, S. He, T. Liu, and K.-L. Wang, *Physical Review A* **86**, 023822 (2012).
- [38] M.-J. Hwang and M. B. Plenio, *Physical Review Letters* **117**, 123602 (2016).
- [39] L. Bakemeier, A. Alvermann, and H. Fehske, *Phys. Rev. A* **85**, 043821 (2012).
- [40] X.-Y. Chen and Y.-Y. Zhang, *Physical Review A* **97**, 053821 (2018).
- [41] See Supplemental Material at [URL_will_be_inserted_by_publisher](#) for more details.
- [42] T. Holstein and H. Primakoff, *Physical Review* **58**, 1098 (1940).
- [43] H. J. Lipkin, N. Meshkov, and A. Glick, *Nuclear Physics* **62**, 188 (1965).
- [44] J. Zhao and M.-J. Hwang, *Physical Review Letters* **128**, 163601 (2022).
- [45] M. Mohylina, J. Buša Jr, and M. Žukovič, *Journal of Magnetism and Magnetic Materials* **527**, 167755 (2021).
- [46] H. D. Rosales, D. C. Cabra, and P. Pujol, *Physical Review B* **92**, 214439 (2015).
- [47] C. Emary and T. Brandes, *Phys. Rev. E* **67**, 066203 (2003).

I. SUPPLEMENTAL MATERIAL: UNDERSTANDING THE QUANTUM RABI RING USING ANALOGIES TO QUANTUM MAGNETISM

In this Supplementary Material, we provide useful details about the derivation of the effective Hamiltonians for the quantum Rabi ring, the mapping between the LMG ring and the quantum Rabi ring, the derivation of the phase boundaries' expressions, a numerical description of the LMG ring phase diagram, and the derivation of the analytical values of the mean-field order parameters of the quantum Rabi ring for the case $N = 4$.

A. Effective Hamiltonians of the quantum Rabi ring

In this section, we derive the effective Hamiltonian of the quantum Rabi ring in the super-radiant phase, given in Eq.(3) of the main text.

As the scaled coupling strength $g_1 = \frac{g}{\sqrt{\Delta\omega}}$ increases to the critical point g_{1c} , photons in each cavity are macroscopically populated. Due to the macroscopic population, the bosonic operator a_n^\dagger (a_n) is expected to be shifted as

$$a_n^\dagger \rightarrow \tilde{a}_n^\dagger + \alpha_n^*, \quad a_n \rightarrow \tilde{a}_n + \alpha_n, \quad (8)$$

with the complex displacement $\alpha_n = A_n + iB_n$. One obtains the Hamiltonian $H_{RR} = H_s + H_1$, which consists of the purely atomic part of the Hamiltonian

$$H_s = \sum_{n=1}^N g (\alpha_n^* + \alpha_n) \sigma_n^x + \frac{\Delta}{2} \sigma_n^z, \quad (9)$$

and the remaining Hamiltonian

$$\begin{aligned} H_1 = & \sum_{n=1}^N \omega (\tilde{a}_n^\dagger + \alpha_n^*) (\tilde{a}_n + \alpha_n) + \sum_{n=1}^N g (\tilde{a}_n^\dagger + \tilde{a}_n) \sigma_n^x \\ & + J \sum_{n=1}^N [(\tilde{a}_n^\dagger + \alpha_n^*) [e^{i\theta} (\tilde{a}_{n+1} + \alpha_{n+1}) + e^{-i\theta} (\tilde{a}_{n-1} + \alpha_{n-1})]]. \end{aligned} \quad (10)$$

To diagonalize H_s , we apply the transformation

$$|+z\rangle = \cos \gamma_n |e\rangle + \sin \gamma_n |g\rangle, \quad |-z\rangle = -\sin \gamma_n |e\rangle + \cos \gamma_n |g\rangle, \quad (11)$$

with $\tan 2\gamma_n = 4gA_n/\Delta$. This leads to the renormalized frequency of the n -th atom

$$\Delta_n = \sqrt{\Delta^2 + 16g^2A_n^2}, \quad (12)$$

and the Pauli matrices can be expressed in the subspace of $\{|+z\rangle, |-z\rangle\}$ as $\tau_z^n = \Delta/\Delta_n \sigma_n^z + 4gA_n/\Delta_n \sigma_n^x$. Thus the Hamiltonian H_{RR} becomes

$$H_{RR} = \sum_{n=1}^N \omega \tilde{a}_n^\dagger \tilde{a}_n + \frac{\Delta_n}{2} \tau_z^n + \lambda_n (\tilde{a}_n^\dagger + \tilde{a}_n) \tau_n^x + J \tilde{a}_n^\dagger (e^{i\theta} \tilde{a}_{n+1} + e^{-i\theta} \tilde{a}_{n-1}) + V'_{off} + E_0,$$

where the effective coupling strength is $\lambda_n = g\Delta/\Delta_n$. The off-diagonal term is

$$V'_{off} = \sum_{n=1}^N \omega (\alpha_n \tilde{a}_n^\dagger + \alpha_n^* \tilde{a}_n) + g (\tilde{a}_n^\dagger + \tilde{a}_n) \sin(2\gamma_n) \sigma_n^z + J [\tilde{a}_n^\dagger (e^{i\theta} \alpha_{n+1} + e^{-i\theta} \alpha_{n-1}) + h.c.], \quad (13)$$

and $E_0 = \sum_{n=1}^N \omega \alpha_n^* \alpha_n + J \alpha_n^* (e^{i\theta} \alpha_{n+1} + e^{-i\theta} \alpha_{n-1})$.

By making off-diagonal term vanish (see below), the transformed Hamiltonian becomes

$$H_{RR} = \sum_{n=1}^N H_{R,n} + J \tilde{a}_n^\dagger (e^{i\theta} \tilde{a}_{n+1} + e^{-i\theta} \tilde{a}_{n-1}) + E_0, \quad (14)$$

where the transformed quantum Rabi Hamiltonian is

$$H_{R,n} = \omega \tilde{a}_n^\dagger \tilde{a}_n + \frac{\Delta_n}{2} \tau_n^z + \lambda_n (\tilde{a}_n^\dagger + \tilde{a}_n) \tau_n^x. \quad (15)$$

We perform a Schrieffer-Wolff transformation with the unitary operator $S_n = \exp[-i\sigma_n^y \lambda_n / \Delta_n (\tilde{a}_n^\dagger + \tilde{a}_n)]$ on the Rabi Hamiltonian $H_{R,n}$ to eliminate the block-off-diagonal interaction $\lambda_n (\tilde{a}_n^\dagger + \tilde{a}_n) \tau_n^x$. In each cavity, the quantum Rabi Hamiltonian is transformed as $H'_{R,n} = S_n^\dagger H_{R,n} S_n$. By performing the second-order correction, the transformed Hamiltonian becomes

$$H'_{R,n} = \omega \tilde{a}_n^\dagger \tilde{a}_n + \frac{\Delta_n}{2} \tau_n^z + \frac{\lambda_n^2}{\Delta_n} (\tilde{a}_n + \tilde{a}_n^\dagger)^2 \sigma_n^z + O\left(\frac{\lambda_n^4}{\Delta_n^4}\right). \quad (16)$$

Using the unitary transformation $U = \prod_n^N S_n$, we obtain the effective quantum Rabi ring Hamiltonian

$$H_{\text{RR}} = \sum_{n=1}^N H'_{R,n} + J \sum_{n=1}^N (e^{i\theta} a_n^\dagger a_{n'} + h.c.) + E_0, \quad (17)$$

where higher-order terms of the second term are neglected for small value of J/ω in the $\Delta/\omega \rightarrow \infty$ limit.

Since the transformed Hamiltonian (17) is free of coupling terms between spin states $|\downarrow\rangle$ and $|\uparrow\rangle$, the lower-energy Hamiltonian is obtained by projecting to the spin subspace $|\downarrow\rangle$, giving

$$H_{\text{eff}}^\downarrow = \sum_{n=1}^N \omega \tilde{a}_n^\dagger \tilde{a}_n - \frac{\lambda_n^2}{\Delta_n} (\tilde{a}_n^\dagger + \tilde{a}_n)^2 + J \tilde{a}_n^\dagger (e^{i\theta} \tilde{a}_{n+1} + e^{-i\theta} \tilde{a}_{n-1}) + E_g, \quad (18)$$

The above Hamiltonian is Eq.(3) of the main text. The ground-state energy is

$$E_g = \sum_{n=1}^N \omega (A_n^2 + B_n^2) - \frac{1}{2} \sqrt{\Delta^2 + 16g^2 A_n^2} + 2J[(A_n A_{n+1} + B_n B_{n+1}) \cos \theta + \sin \theta (B_n A_{n+1} - B_{n+1} A_n)] \quad (19)$$

Which is Eq.(4) of the main text.

B. Effective magnetic model

In this section, we explain the mapping between the paramagnetic phase in the LMG ring and the normal phase in the quantum Rabi ring. We start by noting that in the normal phase $\alpha_n = 0$, and, consequently, $a_n = \tilde{a}_n$. The effective Hamiltonian for the quantum Rabi ring in this phase is simply

$$H_{\text{eff}}^\downarrow = \sum_{n=1}^N \omega a_n^\dagger a_n - g_1^2 \omega (a_n^\dagger + a_n)^2 + J a_n^\dagger (e^{i\theta} a_{n+1} + e^{-i\theta} a_{n-1}), \quad (20)$$

The Lipkin-Meshkov-Glick (LMG) model was proposed initially to describe phase transitions in nuclei [43], and its Hamiltonian is given by

$$H_{\text{LMG}} = -\frac{1}{2S} [\gamma_x (S^x)^2 + \gamma_y (S^y)^2] + h S^z \quad (21)$$

where S^i are the components of a spin operator of length S . If S^i are regarded as collective spins comprised obtained as a sum of individual $1/2$ spins, the first term of the LMG model describes an infinite range interaction between individual spins, whose anisotropy is modulated by parameters γ_x and γ_y . h represents a transverse field interaction.

Now, let's consider that we have a ring with each site labeled by $n = 1, 2, \dots, N$, and each site contains a system described by an LMG Hamiltonian. If interactions between nearest-neighbor LMG systems are allowed, the full Hamiltonian is

$$H_{\text{LMGR}} = \sum_{n=1}^N -\frac{\gamma h}{2S} (S_n^x)^2 + h S_n^z + \frac{\mathcal{J}}{2S} \sum_{n=1}^N (S_n^x S_{n+1}^x + S_n^y S_{n+1}^y) + \frac{1}{2S} \sum_{n=1}^N \vec{D} \cdot (\vec{S}_n \times \vec{S}_{n+1}) \quad (22)$$

where we have set $\gamma_x = \gamma h$ and $\gamma_y = 0$. The third term in Eq. 22 is a conventional XX symmetric spin exchange interaction which can be regarded as ferromagnetic or antiferromagnetic depending on the sign of \mathcal{J} . Additionally, the last term corresponds to the Dzyaloshinskii-Moriya interaction. From now on, we define the vector $\vec{\mathcal{D}}$ to be constant and pointing along the z -direction, namely, $\vec{\mathcal{D}} = (0, 0, \mathcal{D})$.

Here, we are interested in the classical spin limit $S \rightarrow \infty$ mean-field behavior of the model on Eq. 22. In the paramagnetic phase, $\langle S_n^x \rangle = \langle S_n^y \rangle = 0$, the Holstein-Primakoff transformation [42] can be approximated by

$$S_n^z = a_n^\dagger a_n - S, \quad S_n^x \approx \sqrt{\frac{S}{2}}(a_n + a_n^\dagger). \quad (23)$$

Using this form of the Holstein-Primakoff transformation on Eq. 22, one obtains the Hamiltonian

$$H_{\text{eff}} = \sum_{n=1}^N h a_n^\dagger a_n - \frac{\gamma h}{2} \omega (a_n^\dagger + a_n)^2 + a_n^\dagger \left(\left(\frac{\mathcal{J}}{2} + i \frac{\mathcal{D}}{2} \right) a_{n+1} + \left(\frac{\mathcal{J}}{2} - i \frac{\mathcal{D}}{2} \right) a_{n-1} \right), \quad (24)$$

which is exactly the same effective Hamiltonian as the one in Eq. 20 once the parameters are defined as $h = \omega$, $\frac{\gamma}{2} = 2g_1^2$, $\frac{\mathcal{J}}{2} = J \cos \theta$, and $\frac{\mathcal{D}}{2} = J \sin \theta$. With these parameter values the Hamiltonian on Eq. 22 becomes Eq.(5) of the main text. The mapping makes evident that the paramagnetic phase in the LMG ring and the normal phase in the quantum Rabi ring are described by the same effective Hamiltonian.

The classical spin limit mean-field energy of the LMG ring with these parameter values is given by

$$\begin{aligned} \frac{E_{MF}}{\omega S} &= \sum_{n=1}^N -\sqrt{(1 - X_n^2 - Y_n^2)} - 2g_1^2 X_n^2 \\ &\quad + \frac{J}{\omega} \cos \theta (X_n X_{n+1} + Y_n Y_{n+1}) \\ &\quad + \frac{J}{\omega} \sin \theta (X_n Y_{n+1} - X_{n+1} Y_n), \end{aligned} \quad (25)$$

which is Eq.(6) of the main text. Here, $X_n = \langle S_n^x \rangle / S$ and $Y_n = \langle S_n^y \rangle / S$.

C. Analytical expressions for the phase boundaries

The starting point is the effective Hamiltonian on Eq. 20 used to describe the normal phase in the quantum Rabi ring and the paramagnetic phase in the LMG ring. We introduce a Fourier transform defined by $a_n^\dagger = \frac{1}{\sqrt{N}} \sum_q e^{inq} a_q^\dagger$, the effective Hamiltonian is transformed into

$$H_{\text{eff}} = \sum_q \omega_q a_q^\dagger a_q - g_1^2 \omega (a_q a_{-q} + a_q^\dagger a_{-q}^\dagger) - g_1^2 \omega, \quad (26)$$

where $\omega_q = \omega - 2g_1^2 \omega + 2J \cos(\theta - q)$. In order to eliminate the non-diagonal terms we can perform a two-mode squeezing transformation given by $S_q = \exp(\xi_q a_q^\dagger a_{-q}^\dagger - \xi_q^* a_q a_{-q})$, where $\xi_q = r_q e^{i\phi_q}$ being the squeezing parameter. Setting $\phi_q = 0$ and $r_q = \frac{1}{8} \log \left(\frac{\omega_q + \omega_{-q} + 4g_1^2 \omega}{\omega_q - \omega_{-q} + 4g_1^2 \omega} \right)$, the Hamiltonian takes the diagonal form

$$H_{\text{eff}} = \sum_q \epsilon_q a_q^\dagger a_q + E_q, \quad (27)$$

where $E_q = -g_1^2 \omega + \frac{1}{2} \sum_q (\epsilon_q - \omega_q)$, and the excitation energy ϵ_q is given by

$$\epsilon_q = \frac{1}{2} \left(\omega_q - \omega_{-q} + \sqrt{(\omega_q + \omega_{-q})^2 - 16g_1^4 \omega^2} \right). \quad (28)$$

The specific values that q can take, are determined by the size of the ring N . Each superradiant/non-paramagnetic phase is identified by one or more values of q . A second-order phase boundary is found when the gap between the ground state and first excited state vanishes. In the case of a Hamiltonian of the form of Eq. 27 the second order boundary is determined by $\epsilon_q = 0$, which for a specific q gives the boundary equation

$$g_{1c}(q, \theta) = \frac{1}{2} \sqrt{\frac{1 + \frac{4J}{\omega} \cos \theta \cos q + \frac{4J^2}{\omega^2} \cos(\theta + q) \cos(\theta - q)}{1 + 2J/\omega \cos \theta \cos q}}. \quad (29)$$

This value of g_1 signals the second-order boundary between the superradiant/non-paramagnetic phase, characterized by the value q , and the normal/paramagnetic phase. Now, if there are two superradiant/non-paramagnetic phases separated by a phase boundary, and such phases are characterized by q and q' , the value of θ where the triple point separating the three phases occurs is given by

$$g_{1c}(q, \theta) = g_{1c}(q', \theta). \quad (30)$$

In the last section of the Supplementary Material and in the main text we present specific values of θ_c and g_{1c} for $N = 4$.

Now, for the superradiant phases we can conduct a similar procedure as the one just described. Our starting point is now the general effective Hamiltonian on Eq.18. Now, it might seem that doing the Fourier transform is not possible as λ_n and Δ_n depend on n , however, for all the phases in the square lattice (this doesn't follow for $N = 3$) the value of A_n depends on n but the value of A_n^2 is independent of n , and since λ_n and Δ_n depend only on A_n^2 turns out both λ_n and Δ_n are independent of n .

Then, by setting $\lambda_n = \lambda'$ and $\Delta_n = \Delta'$, one can obtain the diagonalized Hamiltonian

$$H_{\text{eff}} = \sum_q \epsilon'_q a_q^\dagger a_q + E'_q, \quad (31)$$

where $E'_q = -\frac{\lambda'^2}{\Delta'} + \frac{1}{2} \sum_q (\epsilon_q - \omega'_q)$, $\omega'_q = \omega - 2\frac{\lambda'^2}{\Delta'} + 2J \cos(\theta - q)$, and the excitation energy ϵ'_q is given by

$$\epsilon'_q = \frac{1}{2} \left(\omega'_q - \omega'_{-q} + \sqrt{(\omega'_q + \omega'_{-q})^2 - 16 \left(\frac{\lambda'^2}{\Delta'} \right)^2} \right). \quad (32)$$

Since now we have expressions for ϵ_q before and after the phase transition boundary g_{1c} , we can plot the behavior around g_{1c} for each value of q and study the scaling exponents of ϵ_q if we represent it as $\epsilon_q \propto |g_1 - g_{1c}(q)|^{\gamma_q}$. For a square lattice $N = 4$ the allowed values of q are $0, \pm\pi/2$ and π . The FSP is associated with $q = 0$, the AFSP with $q = \pi$ and the CSP with $q = \pm\pi/2$. The behavior of ϵ_q around g_{1c} for four fixed values of θ characteristic of each phase is shown in Fig.4.

As shown in the figure $\gamma_q = 1/2$ for $q = 0, \pi$ and $\gamma_q = 1$ for $q = \pm\pi/2$, consistent with the numerical results presented in Fig.(3) of the main text. Note that the exponents agree with the ones in real space presented in Fig.(3) of the main text. The reason why real space diagonalization is needed is because the Hamiltonian 18 for the chiral-phase in the triangle case cannot be Fourier transformed in a similar way as the λ_n^2/Δ_n coefficient is n dependent. The diagonalization in real space, performed to obtain Fig.(3) of the main text, is done as follows.

The effective Hamiltonian for $g_1 > g_{1c}$ in Eq. (3) of the main text bilinear in the creation and annihilation operators a_n^\dagger and a_n . It can be diagonalized by the bosonic Bogoliubov transformation. Denoting $\alpha = \{a_1, a_2, a_3, a_4, a_1^\dagger, a_2^\dagger, a_3^\dagger, a_4^\dagger\}$, the Hamiltonian in Eq. (3) of the main text for $N = 4$ can be written in matrix form as $H_{\text{CP}}^\dagger = \alpha M \alpha^\dagger - 2(\omega - \lambda_n^2)$ with $\lambda_n^2 = \lambda_n^2/\Delta_n$, where the matrix M is given by

$$M(N=4) = \begin{pmatrix} \omega/2 - \lambda_1^2 & J e^{-i\theta}/2 & 0 & J e^{i\theta}/2 & -\lambda_1^2 & 0 & 0 & 0 \\ J e^{i\theta}/2 & \omega/2 - \lambda_2^2 & J e^{-i\theta}/2 & 0 & 0 & -\lambda_2^2 & 0 & 0 \\ 0 & J e^{i\theta}/2 & \omega/2 - \lambda_3^2 & J e^{-i\theta}/2 & 0 & 0 & -\lambda_3^2 & 0 \\ J e^{-i\theta}/2 & 0 & J e^{i\theta}/2 & \omega/2 - \lambda_4^2 & 0 & 0 & 0 & -\lambda_4^2 \\ -\lambda_1^2 & 0 & 0 & 0 & \omega/2 - \lambda_1^2 & J e^{i\theta}/2 & 0 & J e^{-i\theta}/2 \\ 0 & -\lambda_2^2 & 0 & 0 & J e^{-i\theta}/2 & \omega/2 - \lambda_2^2 & J e^{i\theta}/2 & 0 \\ 0 & 0 & -\lambda_3^2 & 0 & 0 & J e^{-i\theta}/2 & \omega/2 - \lambda_3^2 & J e^{i\theta}/2 \\ 0 & 0 & 0 & -\lambda_4^2 & J e^{i\theta}/2 & 0 & J e^{-i\theta}/2 & \omega/2 - \lambda_4^2 \end{pmatrix}. \quad (33)$$

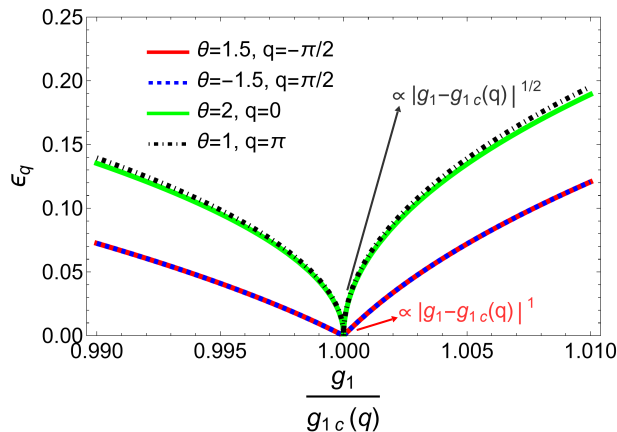


Figure 4. Lowest excitation energy for the different phases of the quantum Rabi square across the second order boundary $g_{1c}(q)$, with $q = 0$ for the FSP, $q = \pi$ for the AFSP and $q = \pm\pi/2$ for the CSP. The scaling exponents of each phase are indicated with arrows, being $1/2$ for the AFSP and FSP, and 1 for the CSP.

We perform a Bogoliubov's transformation to give bosonic operators $\beta = \{b_1^\dagger, b_2^\dagger, b_3^\dagger, b_4^\dagger, b_1, b_2, b_3, b_4\}$ as a linear combination of $\alpha = \{a_1, a_2, a_3, a_4, a_1^\dagger, a_2^\dagger, a_3^\dagger, a_4^\dagger\}$, which satisfies $\alpha^\dagger = T\beta^\dagger$ with a transformation matrix T . To ensure the bosonic commutation relations for the operators, the matrix T satisfies

$$T^\dagger \Lambda T = \Lambda = \begin{pmatrix} I_4 & 0 \\ 0 & -I_4 \end{pmatrix}, \quad (34)$$

where I_4 is the identity matrix with the dimension 4×4 . Substituting for α and α^\dagger in terms of β^\dagger and β , one obtains $H_{\text{cCP}}^\downarrow = \alpha M \alpha^\dagger = \beta T^\dagger M T \beta^\dagger$ in diagonalized form as

$$H_{\text{cCP}}^\downarrow = \beta \varepsilon \beta^\dagger = 2 \sum_{n=1}^4 \varepsilon_n b_n^\dagger b_n + \frac{1}{2} \varepsilon_n, \quad (35)$$

where the matrix ε of the eigenvalues $\{\varepsilon_i\}$ is

$$\varepsilon = T^\dagger M T = \begin{pmatrix} \varepsilon_1 & 0 & 0 & 0 & 0 & 0 & 0 & 0 \\ 0 & \varepsilon_2 & 0 & 0 & 0 & 0 & 0 & 0 \\ 0 & 0 & \varepsilon_3 & 0 & 0 & 0 & 0 & 0 \\ 0 & 0 & 0 & \varepsilon_4 & 0 & 0 & 0 & 0 \\ 0 & 0 & 0 & 0 & \varepsilon_1 & 0 & 0 & 0 \\ 0 & 0 & 0 & 0 & 0 & \varepsilon_2 & 0 & 0 \\ 0 & 0 & 0 & 0 & 0 & 0 & \varepsilon_3 & 0 \\ 0 & 0 & 0 & 0 & 0 & 0 & 0 & \varepsilon_4 \end{pmatrix}. \quad (36)$$

It follows that $T^\dagger M T = \Lambda T^{-1} \Lambda M T = \varepsilon$, resulting in $T^{-1} \Lambda M T = \Lambda \varepsilon$. Hence, the eigenvalues $\pm \varepsilon_i$ are obtained by diagonalizing the matrix ΛM with the matrix M in Eq.(33). Similarly, one can diagonalize ΛM to obtain the excitation energy for $N = 3$.

II. NUMERICAL MEAN-FIELD PHASE DIAGRAM OF THE LMG RING FOR N=3 AND N=4

It's important to note that an effective Hamiltonian for the non-paramagnetic phases of the model on Eq. 22 will, in general, not have the form of Eq. 18. However, as shown in Fig.5 and Figs.(1) and (2) of the main text, the mean-field order parameter values X_n and Y_n found through minimization of Eq.25 are in very good agreement with the phase boundaries found for the quantum Rabi Ring. For both $N = 4$ and $N = 3$ we can observe that the second-order boundaries fit exactly the numerical values of X_n , this is not surprising as we already discussed that both systems share the same second-order boundaries.

It's also helpful to study the behavior of Y_n as a non-zero value of this parameter differentiates the chiral magnetic phase from the other non-paramagnetic phases. We see that as we move deeper in the non-paramagnetic phases

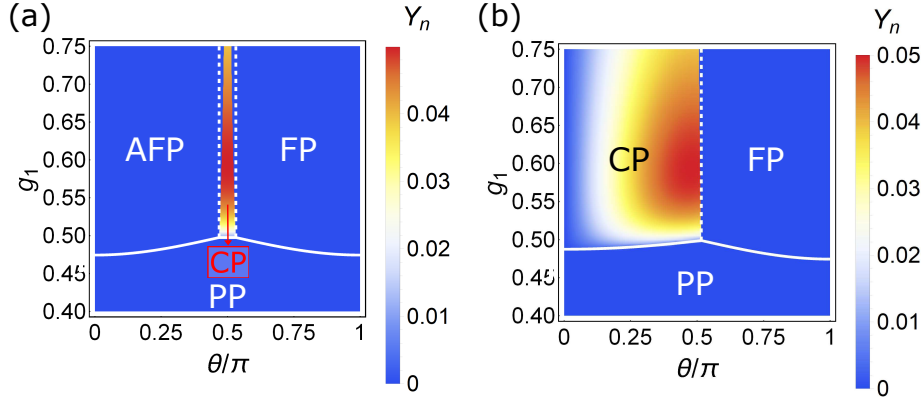


Figure 5. Phase diagram in the $\theta - g_1$ plane for the LMG ring using Y_n for a given site n as order parameter for (a) $N = 4$ and (b) $N = 3$. To facilitate visualization of the different phases we have chosen one of the degenerate configurations of the ground state for each phase, such that $Y_n > 0$ for the chiral phase. The solid white line represents the second-order phase boundary, while vertical dashed lines represent the predicted first-order lines obtained for the equivalent quantum Rabi ring. The hopping strength is set to $J/\omega = 0.05$.

(increasing g_1) the numerical first order boundary starts to deviate from the one predicted in the quantum Rabi ring (vertical dashed line), however, the results are almost identical for a very good portion of the phase diagram. Making the quantum Rabi ring an exciting candidate to study chiral magnetism.

A. Analytical expressions of the order parameter for the quantum Rabi square

In this section, we derive the analytical expression of phase boundaries g_{1c}^F , g_{1c}^{AF} , g_{1c}^C in the ferromagnetic superradiant phase (FSP), anti-ferromagnetic superradiant phase (AFSP) and chiral superradiant phase (CSP), and the critical value θ_c^\pm given in Eq.(7) of the main text, respectively. The analytical solutions are given in detail in the infinite frequency limit $\Delta/\omega \rightarrow \infty$.

It is required that the off-diagonal term V_{off} in Eq.(13) vanishes, which gives

$$\omega\alpha_n - g \sin(2\gamma_n) + J(e^{i\theta}\alpha_{n+1} + e^{-i\theta}\alpha_{n-1}) = 0, \quad (37)$$

One obtains the equations for the real part $Re(V_{off}) = 0$ and for the imaginary part $Im(V_{off}) = 0$

$$\omega A_n - \frac{4g^2 A_n}{\sqrt{16g^2 A_n^2 + \Delta^2}} + J \cos \theta (A_{n+1} + A_{n-1}) + J \sin \theta (B_{n-1} - B_{n+1}) = 0, \quad (38)$$

$$\omega B_n + J \sin \theta (A_{n+1} - A_{n-1}) + J \cos \theta (B_{n+1} + B_{n-1}) = 0. \quad (39)$$

It is equivalent to the equations obtained by minimizing energy in Eq.19 with respect to all A_n 's and B_n 's.

It is easy to obtain $\sum_n Im(V_{off}) = 0$, giving $\omega \sum_n B_n + 2J \cos \theta \sum_n B_n = 0$. This leads to $\sum_n B_n = 0$ and $B_n = -(B_{n+1} + B_{n+2} + B_{n-1})$, and to $\sum_n B_n = 0$. Using the periodic boundary condition $B_{N+1} = B_1$ and $A_{N+1} = A_1$, we obtain the conditions for the even and odd sites as

$$\sum_{k=0} B_{2k+1} = 0, \sum_{k=1} B_{2k} = 0. \quad (40)$$

In particular, when N is odd, there are additional conditions $B_N = -B_1$ and $A_N = A_1$.

Consequently, we obtain the constrain for the imaginary part of α_n for $N = 4$

$$B_{n+1} = -B_{n-1}, B_n = -\frac{J \sin \theta}{\omega} (A_{n+1} - A_{n-1}). \quad (41)$$

By substituting B_n into the Eq.(38), one obtains

$$A_n \left(\omega - \frac{4g^2}{\sqrt{16g^2 A_n^2 + \Delta^2}} - \frac{2J^2 \sin^2 \theta}{\omega} \right) + J \cos \theta (A_{n+1} + A_{n-1}) + \frac{2J^2 \sin^2 \theta}{\omega} A_{n+2} = 0. \quad (42)$$

The analytical solutions of A_n and B_n are derived below.

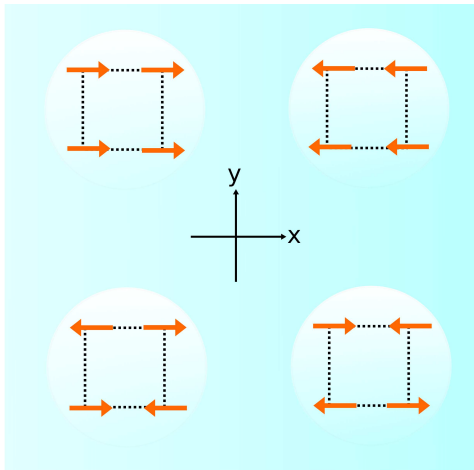


Figure 6. Allowed configurations in the ferromagnetic phase (top row) and antiferromagnetic phase (bottom row). Arrows represent the magnetization on the x-y plane on each site. A similar representation can be done for the ferro-superradiant phase (top) and the antiferro-superradiant phase (bottom) if A_n and B_n are represented in the complex plane.

1. (i) *Ferro/Antiferro-superradiant phase (FSP, AFSP)*

In the FSP and AFSP, all order parameters are real. It implies that $B_n = 0$. According to constraint conditions of B_n in Eq. (41), one has $A_1 = A_3 = a, A_2 = A_4 = a'$. Substituting them into Eq. (42) of A_n leads to

$$a\left(\omega - \frac{4g^2}{\sqrt{16g^2a^2 + \Delta^2}} - \frac{2J^2 \sin^2 \theta}{\omega}\right) + 2Ja' \cos \theta + \frac{2J^2 \sin^2 \theta}{\omega}a = 0, \quad (43)$$

$$a'\left(\omega - \frac{4g^2}{\sqrt{16g^2a'^2 + \Delta^2}} - \frac{2J^2 \sin^2 \theta}{\omega}\right) + 2Ja \cos \theta + \frac{2J^2 \sin^2 \theta}{\omega}a' = 0. \quad (44)$$

One solution is

$$a = a' = \pm \frac{1}{4g} \sqrt{\frac{16g^4}{(\omega + 2J \cos \theta)^2} - \Delta^2}. \quad (45)$$

Setting this equation to zero, one finds the critical strength as $g_{1c}^{\text{FSP}} = \frac{1}{2} \sqrt{1 + 2J/\omega \cos \theta}$, which is consistent with setting $q = 0$ in Eq.29. Then A_n is the same for all four cavities, and hence we call the phase ferro-superradiant phase due to its similarities with a ferromagnetic phase (see Table 1 of the main text).

The other solution is

$$a = -a' = \pm \frac{1}{4g} \sqrt{\frac{16g^4}{(\omega - 2J \cos \theta)^2} - \Delta^2}, \quad (46)$$

Which leads to the critical coupling strength $g_{1c}^{\text{AFSP}} = \frac{1}{2} \sqrt{1 - 2J/\omega \cos \theta}$, consistent with setting $q = \pi$ in Eq.29. In this phase $A_1 = A_3 = -A_2 = -A_4$, which mimics an antiferromagnetic order, hence, we call the phase antiferro-superradiant phase.

Fig. 6 shows a schematic representation of the allowed degenerate configurations in the AFSP and FSP.

2. (ii) *Chiral superradiant phase (CSP)*

In the CSP, α_n is complex and depends on n . Considering $B_n \neq 0$, we have $A_1 \neq A_3$ and $A_2 \neq A_4$. It includes two kinds of solutions $A_1 = A_4 = a, A_2 = A_3 = a'$ and $A_1 = A_2 = a, A_3 = A_4 = a'$. For the first case $A_1 = A_4 = a, A_2 =$

$A_3 = a'$, equations of A_n reduce to

$$a\left(\omega - \frac{4g^2}{\sqrt{16g^2a^2 + \Delta^2}} - \frac{2J^2 \sin^2 \theta}{\omega}\right) + J \cos \theta(a + a') + \frac{2J^2 \sin^2 \theta}{\omega}a' = 0, \quad (47)$$

$$a'\left(\omega - \frac{4g^2}{\sqrt{16g^2a'^2 + \Delta^2}} - \frac{2J^2 \sin^2 \theta}{\omega}\right) + J \cos \theta(a' + a) + \frac{2J^2 \sin^2 \theta}{\omega}a = 0. \quad (48)$$

One solution is

$$a = -a' = \pm \frac{1}{4g} \sqrt{\frac{16\omega^2 g^4}{(\omega^2 - 4J^2 \sin^2 \theta)^2} - \Delta^2}. \quad (49)$$

It leads to the critical coupling strength $g_{1c}^{\text{CSP}} = \frac{1}{2} \sqrt{1 - 4J^2/\omega^2 \sin^2 \theta}$, consistent with setting $q = \pm\pi/2$ in Eq.29. The values of the imaginary parts are

$$B_1 = \frac{2J \sin \theta}{\omega} a' = B_2.$$

It is equivalent to the solution of the case with $A_1 = A_4 = a', A_2 = A_3 = a$.

On the other hand, for the second case $A_1 = A_2 = a, A_3 = A_4 = a'$, one obtains

$$a\left(\omega - \frac{4g^2}{\sqrt{16g^2a^2 + \Delta^2}} - \frac{2J^2 \sin^2 \theta}{\omega}\right) + J \cos \theta(a' + b) + \frac{2J^2 \sin^2 \theta}{\omega}a' = 0, \quad (50)$$

$$a'\left(\omega - \frac{4g^2}{\sqrt{16g^2a'^2 + \Delta^2}} - \frac{2J^2 \sin^2 \theta}{\omega}\right) + J \cos \theta(a' + a) + \frac{2J^2 \sin^2 \theta}{\omega}a = 0. \quad (51)$$

The solutions of a and a' are the same as the above results of the first case. But the values of imaginary parts are different

$$B_1 = -\frac{2J \sin \theta}{\omega} a' = -B_2. \quad (52)$$

Fig. 2 of the main text shows the four allowed configurations in the CSP.